UV photo-sensing performance of NiSnO$_3$ thin films deposited by pulsed spray pyrolysis technique

F G El Desouky, I Moussa and M Obaida*

Solid State Physics Department, Physics Research Institute, National Research Centre, 33 El Buhouth St., Dokki, Cairo 12622, Egypt

Abstract: Pure nanostructured thin films of nickel stannite (NiSnO$_3$; NSO) semiconducting oxide are synthesized by a simple pulsed spray pyrolysis technique on glass substrates at different deposition temperatures and spray times. XRD recorded patterns exhibit a polycrystalline nature for the deposited films. The Raman spectra provide confirmation of the presence of Sn–O and Ni–O bands. FESEM demonstrates a membrane-like structure with hexagonal pores' formation and different diameter sizes. The NSO energy bandgap is calculated to be 3.72 eV using the absorption spectrum fitting method. The photoluminescence intensities of NSO films were found to fluctuate with the influence of deposited substrate temperature and spray time. The photo-sensing performance was examined by calculating the change in the resistance of the deposited films corresponding to the UV light exposure at room temperature. NSO samples prepared at high substrate temperatures, and long spray times perform the best dynamic photo-response for the UV illumination.

Graphical abstract
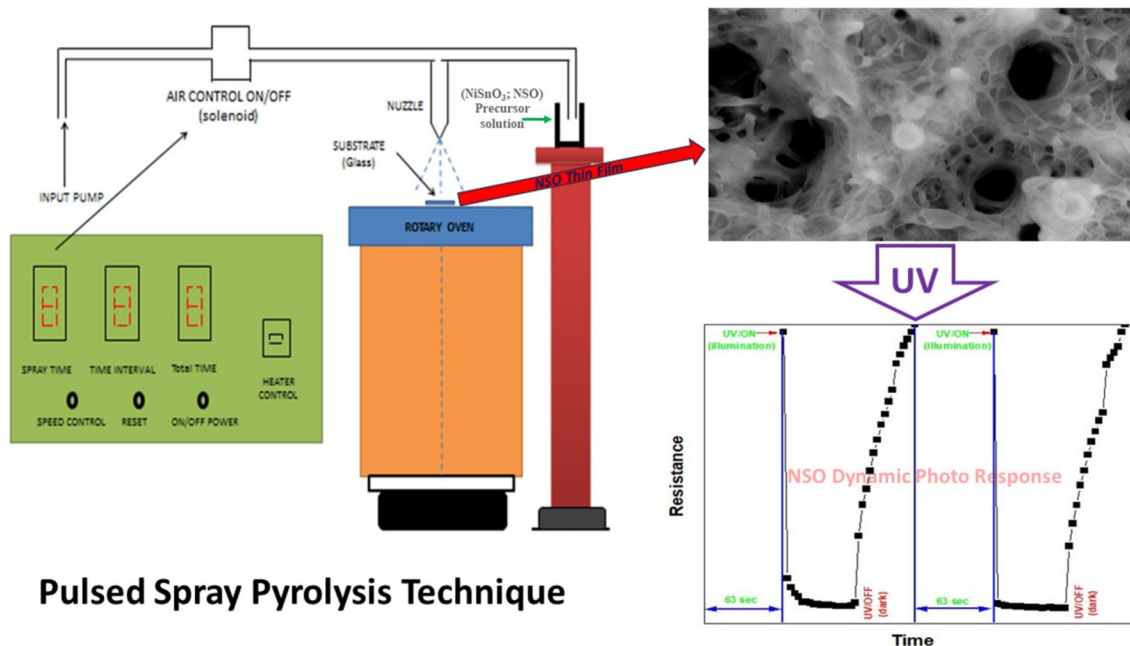
*Corresponding author, E-mail: mz.obaida@nrc.sci.eg

1. Introduction

Due to their exceptional properties, bimetal oxide materials with a crystalline structure of (ABO$_3$, where A and B are two cations) have demonstrated superior capabilities in manipulating their electronic properties compared to nanostructured metal oxide constituents such as NiO, ZnO, and SnO$_2$ [1, 2]. The perovskite-type lattice has a high absorption coefficient, long-range ambipolar charge transport, a low exciton-binding energy, a high dielectric constant, ferroelectric characteristics, etc. Perovskite as a binary transition metal oxide compound has gained more importance in the past few years due to its use in many technical applications such as electrocatalysts [3], chemical gas sensors [4], Li-ion batteries [5], and fuel cell electrodes [6] and supercapcitor electrodes [7]. It has been noted that the poor electrical conductivity of transition metal oxides such as WO$_3$, SnO$_2$, NiO, and TiO$_2$ lowers their specific capacitance, and the electrical conductivity of these nanostructured materials can be improved by creating a mixture of these transition metal oxides [8, 9]. Due to their excellent conductivity performance, cobalt–nickel oxide, nickel–manganese oxide, and cobalt–manganese oxide composites are extensively researched in the literature [10–13].

The lack of reported research on composites of NiO and SnO$_2$ in the literature may be related to that SnO$_2$ (undoped) material has high resistivity (low direct electron transfer rate) [14–16]. The conductive type of MSnO$_3$ (M = Zn, Cd, Ni) perovskite structure was found to be n-type semiconductors, as reported in Ref. [17]. Recently, NiSnO$_3$ (NSO) bimetal oxide has attracted a lot of attention due to its potential applications as a superior electrocatalyst, electrochemical supercapacitors, photovoltaic electrodes, and gas sensors [18–20]. Nanostructured NiSnO$_3$, is a significant perovskite material having a bandgap of 3.75 eV in the visible wavelength region. Moreover, NiSnO$_3$ outperforms single metal oxides (NiO, SnO$_2$) and mixtures of NiO /SnO$_2$ in electrochemical reactions [21]. Several methods are used to prepare bimetal oxides, such as the hydrothermal method [3], cost-effective ultrasonic-assisted method [5], green synthesis method [18], spray pyrolysis [19], chemical coprecipitation technique [17], in situ polymerization method [22], and the co-deposition method [23]. Moreover, most perovskite oxides exhibit semiconductor properties, characterized by wide bandgap energies and unique optical properties. As a result, they are well suited for applications in advanced optoelectronics, photoluminescence (PL), and electroluminescence materials. Nevertheless, despite the abundance of research conducted on perovskite oxide semiconductors, the luminescent properties and dynamics of the excited state are still not understood [24–26]. Since no more have been surveyed and there is a lack of further research work concerning NiSnO$_3$ thin films and their photo-sensing properties. The aim of this work is to focus on the synthesis and stabilization of NiSnO$_3$ thin films on glass substrates by a pulsed spray pyrolysis (PSP) system at a series of different deposition temperatures and spray times. The investigation emphasizes the structural, optical, and photoluminescence features of these deposited films and their performance toward UV light as a promising photo-sensing candidate.

2. Experimental details

Simple pulsed spray pyrolysis (PSP-On/Off) system is used to deposit NiSnO$_3$ (NSO) thin films onto a normal microscopic soda lime glass substrates at different deposition temperatures and spray times, a description of the experimental PSP setup utilized to create the spray-deposited films is mentioned clearly in Ref. [2]. Precursors for nickel and tin were NiCl$_2$.6H$_2$O (purity 97%) and SnCl$_4$.5H$_2$O (purity 98%) of (Sigma-Aldrich). All the chemicals used are grade-mark and were supported without any further decontamination. To create the final spraying solution of 0.1 M concentration with 50 ml for each deposition, an equimolar of (NiCl$_2$.6H$_2$O: SnCl$_4$.5H$_2$O, 1:1) precursors was dissolved in distilled water (D.W.) and vigorously stirred for 20 min to produce the spray deposition solution. NSO thin films were deposited at substrate temperatures of (400, 450 & 500 °C) and spray time (30, 40 & 60 min) with an intermitted pulse deposition interval of (1 s on /4 s off)) for the best obtained deposition temperature condition. All other pulsed spray pyrolysis parameters such as substrate/nozzle distance (28 cm), carrier-gas flow rate (Air 25 L/min), solution molarity. To clarify the existing phases and crystal nature of the deposited films, the X-ray diffractometer (XRD–Empyrean from PANalytical Netherlands) is used to record the XRD patterns for the analyzed samples with 2θ scan angle range between 10° and 80°. The Raman spectra were obtained using the Confocal Raman Microscope (Alpha300 RA/S manufactured by WITec GmbH.), which is aligned through a 20X ZEISS objective to confirm the layer structure and phase formation of the deposited films. To determine the concentration and chemical environment of the samples, the spectrofluorometer (model-FS5) from (Edinburgh Instruments Ltd., UK) is used to analyze their fluorescence characteristics. Field emission scanning electron microscope (FESEM–Quanta FEG 250 with field emission gun, FEI company-The Netherlands) is used to examine the surface morphology of the synthesized thin films, and energy-dispersive X-ray spectroscopy (EDX) tool associated with the FESEM is also used to provide elemental

microanalysis of the prepared samples. The optical transmittance measurements of the films have been examined by UV–Vis–NIR double-beam spectrophotometer (Jasco-750 V) in the wavelength range of 200–2500 nm to estimate the bandgap (E_g) of the films. Photosensitivity (film resistance loss) measurements for NSO films prepared at different conditions were investigated at room temperature. By using UV light lamp (SPECTROLINE model 11SC-1 OP) of (λ = 254 nm & I = 5 mW/cm^2), at different exposure cycles of (ON, illumination / OFF, dark) modes with a computerized interface connected digital multimeter (Tekpower TP4000zc-RS232), and at constant distance of (1 cm) from the UV light source the dynamic photosensitivity of (response/recovery) were recorded directly for the synthesized samples.

3. Results and discussion

3.1. XRD measurements

Figure 1(a, b) shows the XRD spectra of NiSnO₃ (NSO) thin films deposited at different temperatures and times on glass substrates with a 1:1 ratio of Ni to Sn.

Figure 1(a) shows the XRD pattern of the synergistic effect for the samples deposited at constant spray time of 60 min and different deposition temperatures of 400, 450, and 500 °C of the NSO thin films. At deposition temperature of 400 °C, the material exhibits a limited degree of crystallinity, and the observed diffraction patterns can be attributed to the cubic perovskite-type structure of NSO. Specifically, two peaks are found at 2 theta angles of 26.2° and 37.58°, which correspond to the standard diffraction pattern of NSO as documented in the JCPDS database (No: 28-0711) [19, 20, 27]. The enhancement of deposition substrate temperatures to 450 and 500 °C, while maintaining a growth time of 60 min, leads to significant improvements in the crystalline quality of the thin films. At 500 °C, all diffraction patterns of NSO are clearly observed, indicating the polycrystalline nature of the film. Figure 1(a) illustrates a notable increase in the crystalline structure of the film at a temperature of 500 °C compared to all other films deposited at lower temperatures if 400 and 450 °C which reflects that the prepared sample achieved an optimal state of growth. There were no observable diffraction signals indicating additional contamination, thereby affirming the remarkable precision of the produced samples, and bolstering their accuracy. Figure 1(b) elucidates the impact of varying deposition times (30, 40, and 60 min) on the formation of NSO films at a consistent temperature of 500 °C.

For the samples deposited at spray time of 30 min, the recorded diffraction peaks are observed at 2-theta position is very close to 26.14° along the (103) plane and at 37.7° along the (301) plane [3]. Additionally, these weakly observed indicate the presence of a cubic NSO phase and confirm the monocrystalline nature of the synthesized NSO layers. By increasing the deposition time beyond 40 min, the intensity of the diffraction peaks demonstrates a rise when the duration of growth reaches 60 min with a clear polycrystalline arrangement. The results indicate that both substrate temperature and deposition time are conducive to the crystallization of the film. The chemical composition of the NSO thin films depicted in Fig. 1(a) and (b) exhibited minimal or negligible phase transitions as reported from the obtained XRD patterns. Scherer formula in Eq. (1), microstrain strain (ε) in Eq. (2), and dislocation density (δ) in Eq. (3) are used to determine the structure parameters of the specimens, considering the most distinct peak (103) are recorded in Table 1.

$$C = \frac{K\lambda}{\beta \mathrm{Cos}(\theta)}, \tag{1}$$

$$\varepsilon = \frac{\beta}{4\mathrm{Tan}(\theta)}, \tag{2}$$

$$\delta = \frac{1}{C^2}. \tag{3}$$

where λ is the wavelength of Cu Kα radiation of 1.5408 Å, the Scherrer constant k = 0.94, and β is the full width at half maximum (FWHM). The crystallite sizes of the samples deposited at different temperatures of 400 °C, 450 °C & 500 °C and constant spray time of 60 min were determined to be 29.43, 39.50, and 49.12 nm, respectively. These measurements were also investigated for the samples sprayed at constant temperature of 500 °C and different spray times of 30 & 40 min, resulting in crystallite sizes of 25.91 and 30.13 nm. According to the structural parameters obtained in Table 1, the optimal structural characteristic is observed for the NSO film prepared at long spray time and high deposition temperature.

3.2. Raman study

In Fig. 2, an inset shows the Raman spectra of NiSnO₃ (NSO) thin films deposited on glass substrates at different temperatures and spray times. In comparison to X-ray diffraction (XRD) analysis, which exhibits limited sensitivity in detecting low levels of oxide, the utilization of Raman spectroscopy has demonstrated its potential in detecting and characterizing microstructural features as well as identifying defects such as oxygen vacancies.

Consequently, this technique can significantly contribute to the knowledge of various emerging physical phenomena observed in thin films [28]. As depicted in Fig. 2 as an inset, the observed fluctuations in the strength of these

Fig. 1 XRD spectra of NiSnO₃ (NSO) thin films (**a**) deposited at different deposition temperatures of (400, 450, 500 °C & constant spray time of 60 min.) and (**b**) of different spray times at (30, 40, 60 min & constant deposition temperature of 500 °C) on glass substrates
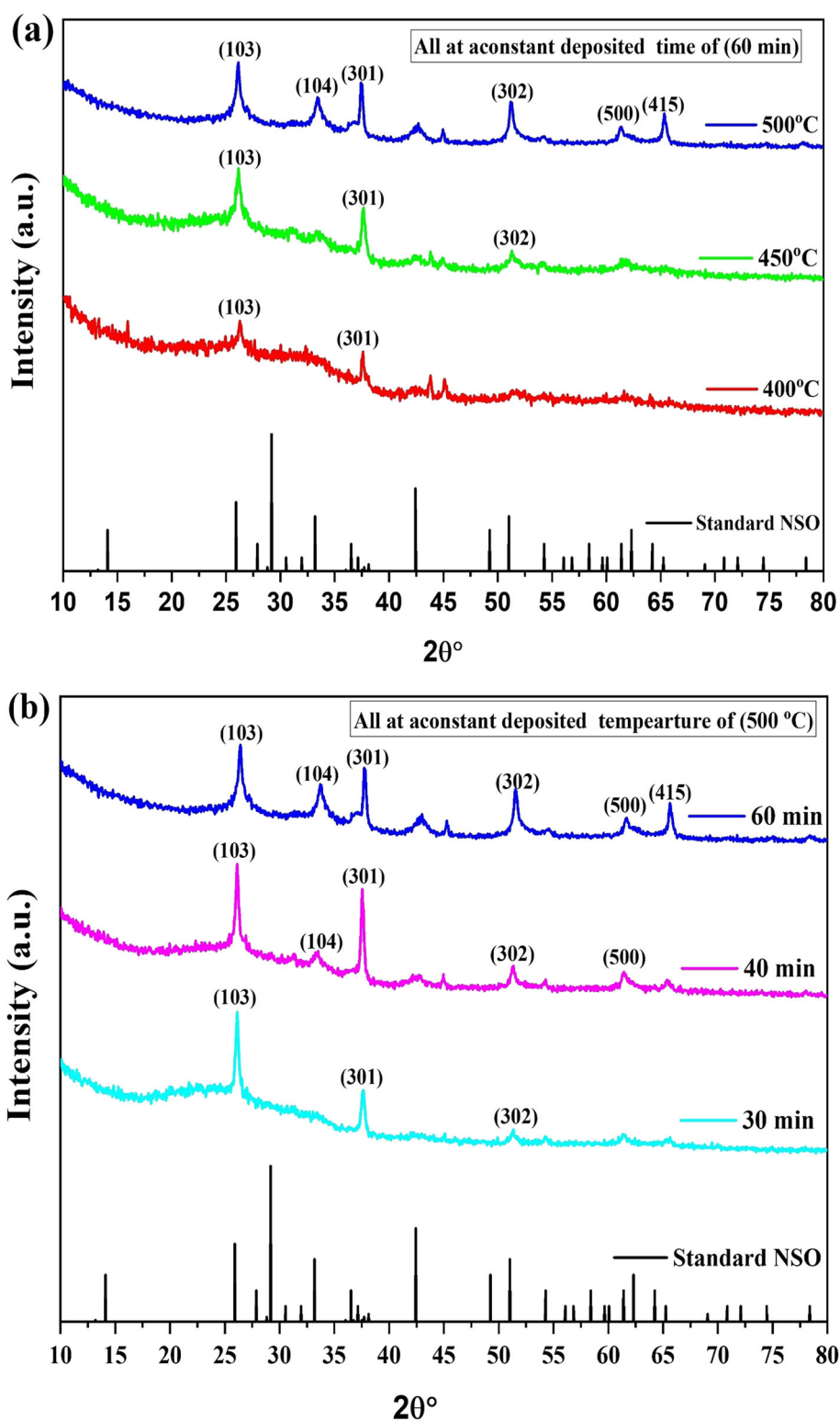
Raman peaks can be attributed to the structural features and size variations of the crystallites, as determined by the XRD analysis provided above. Gaussian fit deconvolutions were conducted on spectra collected from samples to get more accurate Raman line positioning. This is illustrated in

Figs. 3 and 4, where the red lines depict the cumulative fit to the data within the spectral range. Figure 3 illustrates the Raman spectra of a glass substrate, specifically a microscopic slide. The spectrum exhibits two prominent bands at

Table 1 The estimated structural factors, crystallite size C, strain ε and dislocation density δ, of NSO deposited films

Sample	Structural parameters		
	Crystallite size (C) (nm)	Dislocation $\delta*10^{-4}$	$\varepsilon*10^{-3}$
400 °C	29.43	11.54	31.66
450 °C	39.50	6.41	14.98
500 °C	49.12	4.14	8.56
30 min	25.91	14.89	33.64
40 min	30.13	11.01	28.51

wavenumbers of 556 and 1097 cm⁻¹, along with a very small, broad band at 789 cm⁻¹.

The Raman spectra of the NSO thin film, as depicted in Fig. 3, exhibit the presence of four broad peaks when analyzed using Gaussian fit deconvolutions. The thin film was deposited at temperatures of 400 and 450 °C. The spectral peak observed at 527.62 cm⁻¹ may correspond to the formation of glass substrate at a temperature of 400 °C. Additionally, the peaks observed at 554.83 cm⁻¹, 582.88 cm⁻¹, and 630 cm⁻¹ could be related to the presence of the glass substrate and the vibrations of the Ni–O and Sn–O bands [29]. The Raman spectra of the NiSnO₃ (NSO) thin films deposited at different times show three strongest peaks as depicted in Fig. 4. One of these peaks is broad and laying in the range of (562.79–570.21) cm⁻¹, which is related to the tin–oxygen (Sn–O) stretching mode [30, 31]. There are also two-phonon modes at 664.45, 698.75, 753.91, 759 cm⁻¹ (2TO modes) and another at

1066.62, 1081.49, 1088.85, 1093.86, 1089.38 cm⁻¹, associated with nickel oxide (2LO modes) and O–Sn–O, respectively [30–32]; as shown in Figs. 3 and 4. The Raman spectra of the NiSnO₃ (NSO) thin films, which were deposited on glass substrates at various time intervals, exhibit three prominent peaks, as depicted in Fig. 4.

One of these peaks, spanning the range of 562.79–570.21 cm⁻¹ is characterized by its broad nature and is associated with the stretching mode of tin–oxygen (Sn–O) bonds [30, 31]. Additionally, there exist two-phonon modes at frequencies of 664.45, 698.75, 753.91, and 759 cm⁻¹, referred to as 2TO modes. Furthermore, there is another mode at frequencies of 1066.62, 1081.49, 1088.85, 1093.86, and 1089.38 cm⁻¹, connected with nickel oxide (2LO modes) and O–Sn–O, as depicted in Figs. 3 and 4 [30–32].

3.3. FESEM morphological measurements

Figure 5 shows the FESEM images of the sprayed NiSnO₃ perovskite thin film at different deposition temperatures and spray times at a magnification of 50,000×. The films deposited at 400 °C show a poor semi-closed surface morphology, as seen in Fig. 5(a). With increasing deposition temperatures to 450 °C, a preliminary defined film surface morphology improvement starts to appear with the formation of interconnected flakes, as shown in Fig. 5(b).

Finally, NSO films deposited at 500 °C and 60 min show a well-texturally agglomerated interconnected flake of a membrane-like structure, as represented in

Fig. 2 The Raman spectra of NiSnO₃ (NSO) thin films deposited at different deposition temperatures of (400, 450, 500 °C & constant spray time of 60 min.) and different spray times of (30, 40, 60 min & constant deposition temperature of 500 °C)
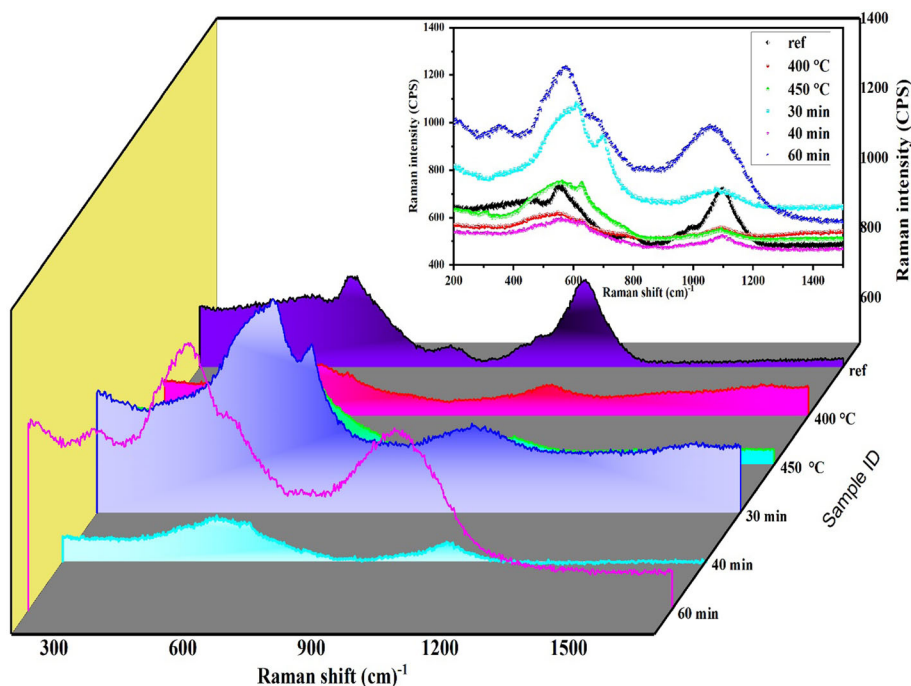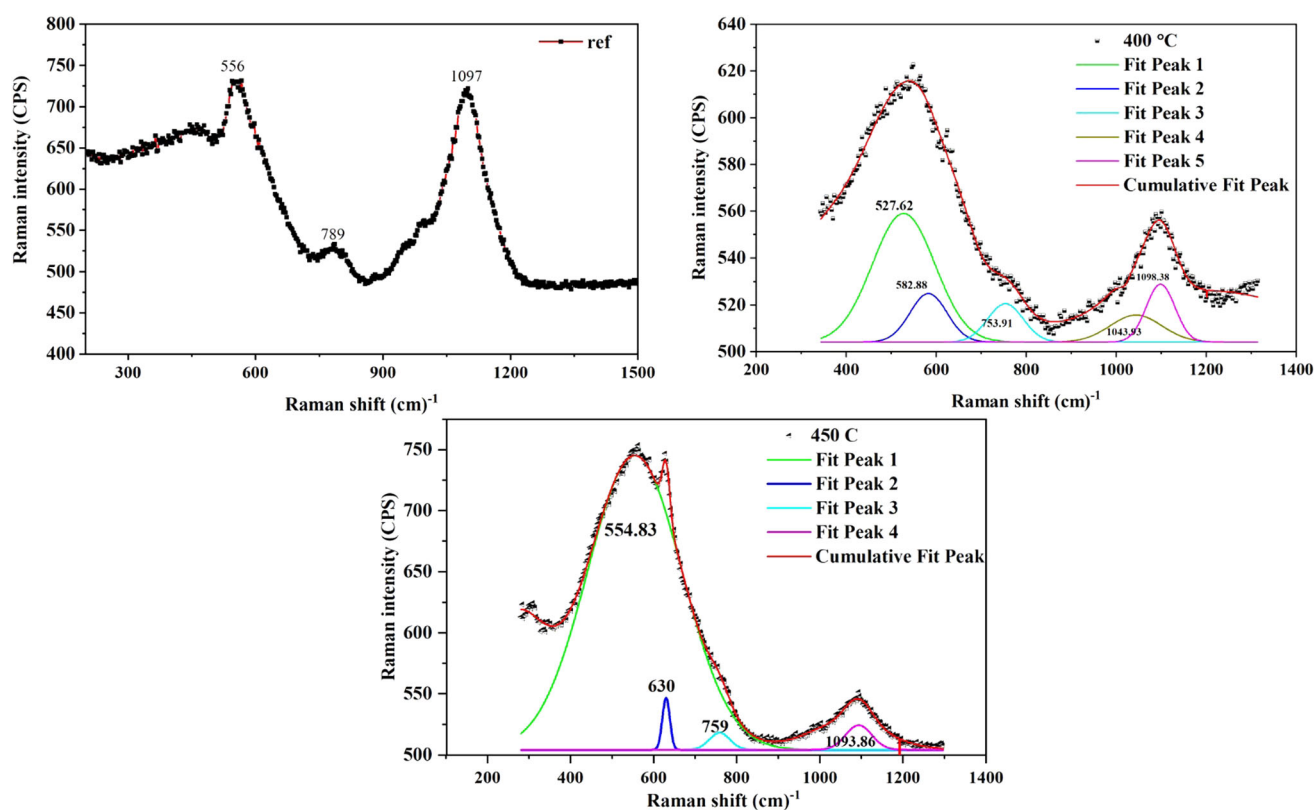
Fig. 3 Gaussian-resolved components of the Raman spectra of NiSnO₃ (NSO) thin films deposited different deposition of temperatures at 400 & 450 °C at constant spray time of 60 min

Fig. 5(e) with a hexagonal pores structure of diameter size within the film texture. For the samples deposited at constant substrate temperature of 500 °C and different spray time of (30 & 40 min), as shown in Fig. 5(c & d), a lower morphological structure for the films prepared at short spray time of 30 min, which enhances to form an interconnected flakes and pores with increasing the spray time to 40 min. Such pore structure is obtained at highly deposited temperature samples, which is related to the film formation based on the nucleation and coalescence of atoms during the deposition process [33].

This type of morphological structure for the prepared samples with this porosity provides a high surface area, which makes it suitable for use in photo-sensor applications [21]. Ni–Sn–O thin film elemental compositions for the best preparation conditions of deposition temperature 500 °C and 60 min spray time are examined by EDX analysis, as illustrated in Fig. 5(f). From the recorded patterns, it is seen that the ratio of Ni:Sn:O is (20.82:17.93:61.26) which confirms the presence of Ni and Sn in the Ni–Sn–O matrix. These average Ni and Sn atomic percentages were recorded at different zones of the NiSnO₃ sprayed sample. This noticeable small excess in the Ni percentage may appear due to the precursor preparation or

the sample deposition process which causes a nonstoichiometric nature in the films, as reported in Ref. [34].

3.4. Optical measurements

NiSnO₃ thin films' optical transmission spectra were investigated using a UV–Vis-NIR spectrophotometer in the range between 0.2 and 2.5 µm. As shown in Fig. 6(a), the deposited films exhibit high transparency within the visible range, with an average transmittance of 65% for the sample deposited at 500 °C and a short spray time of 30 min. While the samples deposited for long spray times of 40 and 60 min showed a low transmittance value; this is due to the increase in the thickness of the films. This implies that these films have a respectable optical quality because of their lowest scattering or absorption losses. The optical bandgap of the prepared samples at different deposition temperatures and spray times was calculated using Tauc's model and the absorption spectrum fitting (ASF) method reported in Ref. [35].

The determined bandgap with this method requires only the measurement of the absorbance spectrum and no additional information, such as the film thickness or reflectance spectra [35]. Since the value of the bandgap, in
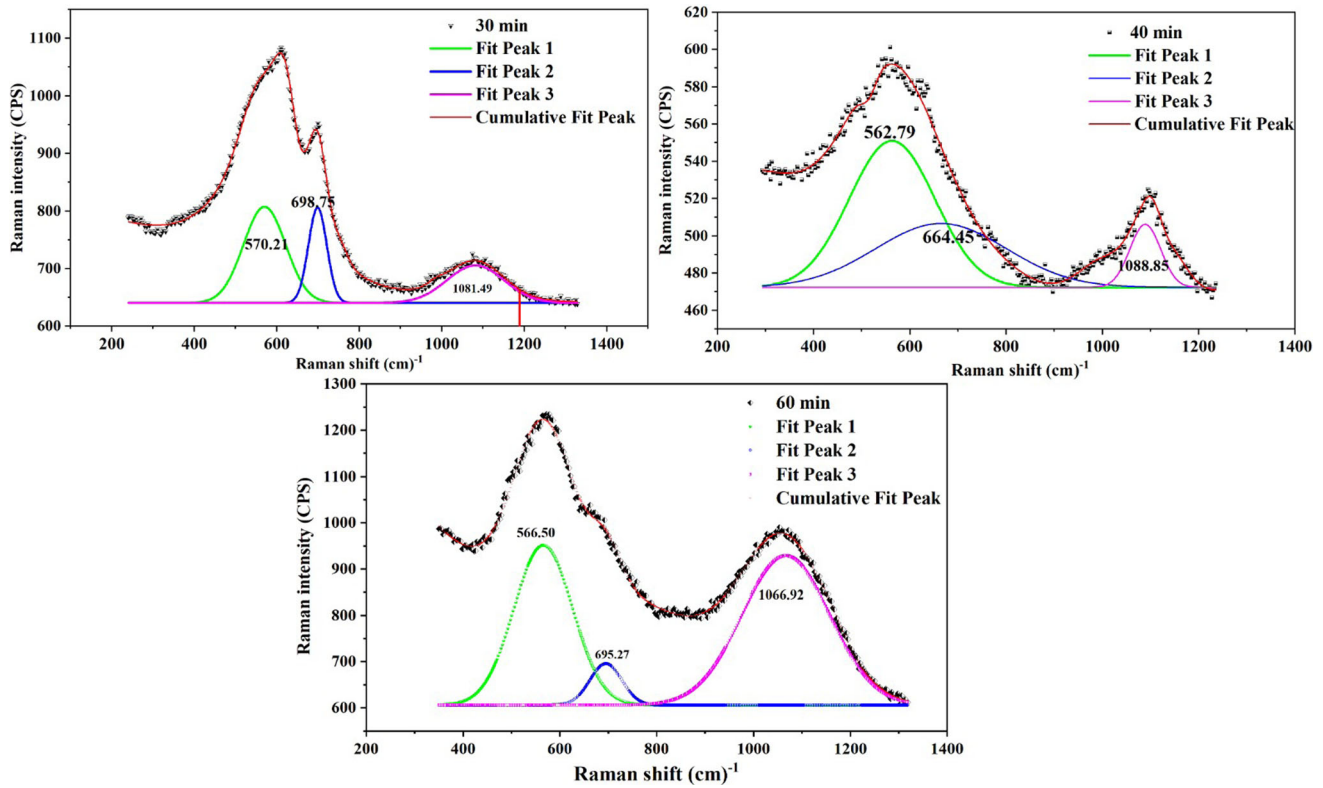
Fig. 4 Gaussian-resolved components of the Raman spectra of NiSnO$_3$ (NSO) thin films deposited at different spray times of (30, 40, 60) minutes at constant deposition temperature of 500 °C

electron volts (eV), can be calculated from the parameter λ_g using the following Eq. (4):

$$E_{gap}^{ASF} = \frac{1239.83}{\lambda_g}. \tag{4}$$

where the value of λ_g can be extrapolated from the linear of the $\left(\frac{Abs(\lambda)}{\lambda}\right)^{\frac{1}{m}}$ versus $(1/\lambda)$ curve at $\left(\frac{Abs(\lambda)}{\lambda}\right)^{\frac{1}{m}} = 0$; in mean absorption range indicating that the electronic transitions are direct [35]. The calculated bandgap values for the prepared samples at a deposition temperature of 500 °C and 60 min of spray time as shown in Fig. 6(b) ranges between 3.59 to 3.72 eV, which are in good agreement with the literature reported in Refs. [7, 34]. The reasons for the shift of the bandgap to lower values are ascribed to the increase in the crystallite size of the particles with increasing deposition time, and also, in these binary metal complex systems, the bandgap in semiconductors becomes narrow due to the redistribution of the charge carriers and their concentration [36, 37].

3.5. Photoluminescence study

Photoluminescence serves as a valuable technique for elucidating the spatial distribution of electron–hole pairs, assessing the efficacy of charge carrier trapping, and evaluating the mobility characteristics of particles within a semiconductor material. The examination of photoluminescence (PL) spectra is vital due to the predominant role of free carrier recombination in causing PL emission. The photoluminescence (PL) spectra of nanostructured materials are intricately linked to the behaviors of photo-induced electron and hole transport. The utilization of these spectra enables the determination of the spatial distribution of electron–hole pairs within semiconductor nanoparticles, as well as the evaluation of the recombination rate of charge carriers [38, 39]. Figure 7(a) and (b) displays the phenomenon of band-to-band emission, which facilitates the direct recombination process between an electron in the conduction band and a hole in the valence band.

Unlike direct recombination, excitonic emission uses flaws and defects on the surface of the substance. The spectral data were partitioned into two distinct regions: the ultraviolet (UV) region and the visible light range, which exhibited a prominent band associated with defects spanning from 468 to 590 nm. The UV emission band-to-band and exciton recombination centered at 369.65 and 381.46 nm, respectively, in NSO is attributed to band-to-band recombination, namely near-band edge excitonic emission, occurring within the large bandgap that agrees with the optical analysis and other reports [19]. The
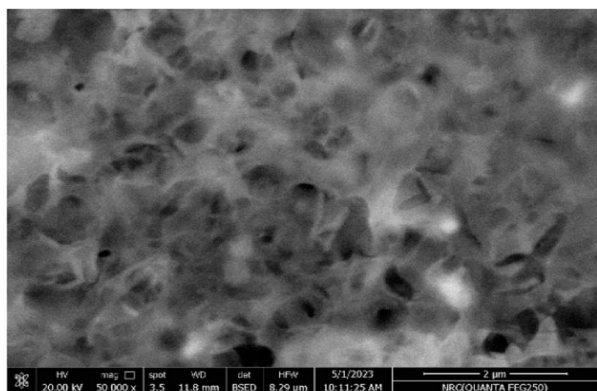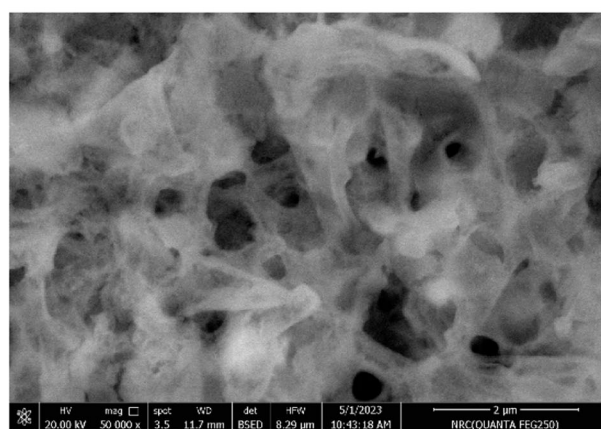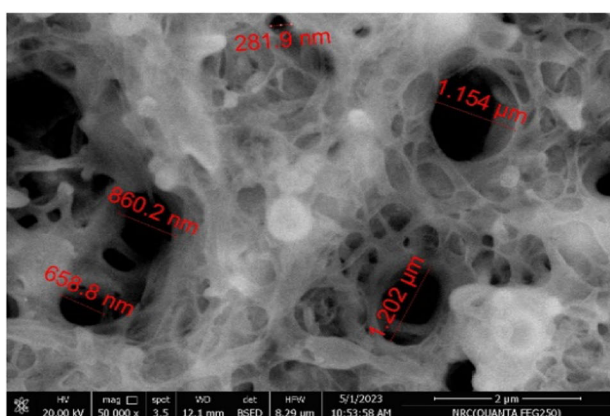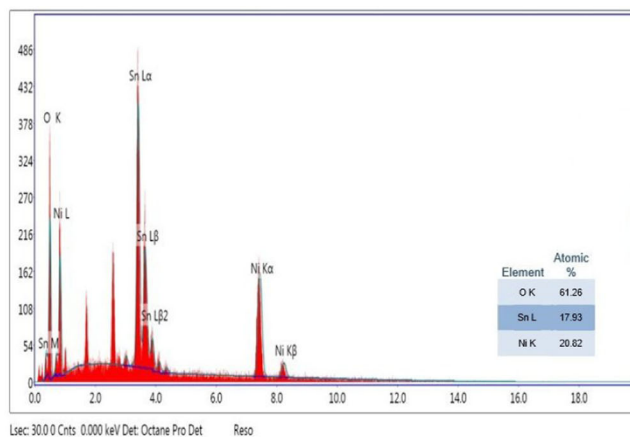
(a) 400°C, 60 min
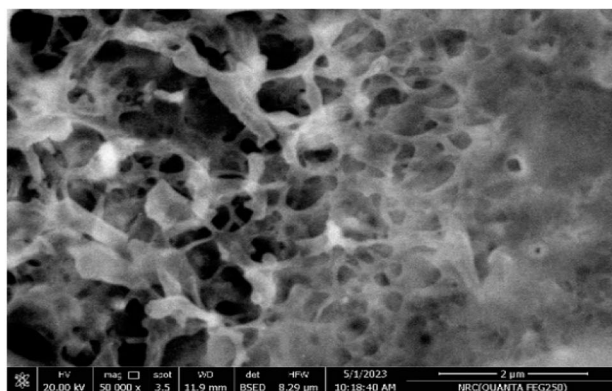
(b) 450°C, 60 min
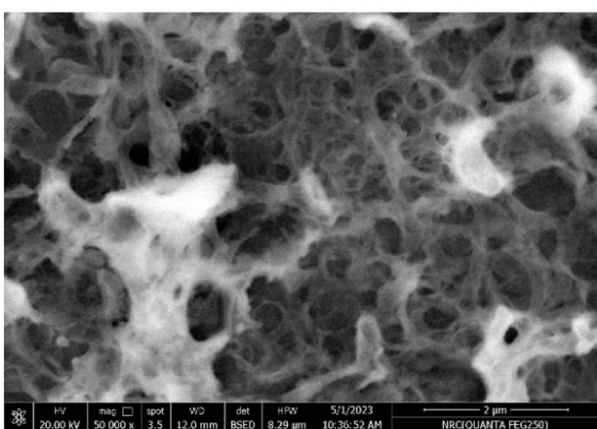
(c) 500°C, 30 min.

(d) 500°C, 40 min.

(e) 500°C, 60 min.

(f) EDX spectrum for sample 500°C, 60 min.

Fig. 5 FESEM micrographs (**a, b, and e**) for the prepared NiSnO$_3$ thin films deposited at different temperatures of (400, 450, 500 °C & constant spray time of 60 min.) and (**c, d, and e**) different spray times of (30, 40, 60 min. & constant deposition temperature of 500 °C). (**f**) EDX images for the best condition deposited sample temperature at 500 °C and spray time of 60 min

Fig. 6 (**a**) The optical transmittance measurement and (**b**) the determined bandgap plots using the ASF method for the samples of 30-, 40-, and 60-min spray time deposited at constant temperature of 500 °C
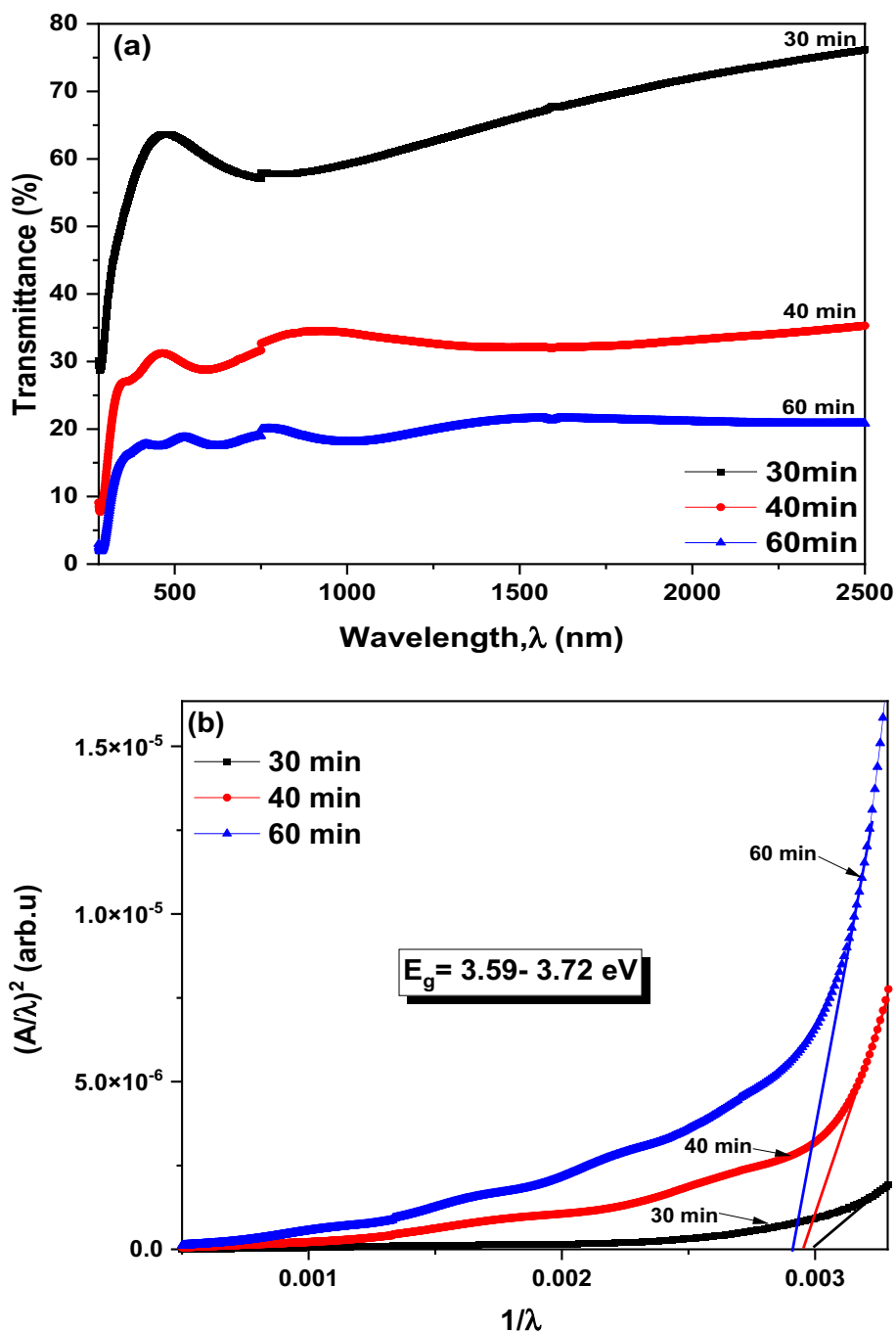

$NiSnO_3$ crystal lattice exhibits violet emission bands at 431 and 437 nm, a blue emission band at 468–469 nm, and green emissions at 509.57 nm, 510 nm, 535 nm, and 545 nm. These emissions are likely associated with the presence of different intrinsic defects when excited at wavelengths of 300 and 350 nm [19]. Additionally, a yellow emission peak is observed at a wavelength of 594 nm.

The origins of both peaks can be attributed to defects or defect levels associated with oxygen vacancies, nanocrystal grains, or tin interstitials that were created by the tin dioxide thin film at the nanoscale [40]. This observation was determined after conducting an analysis of the data. The study conducted by Jiang et al. centered on the examination of photoluminescence of nickel oxide thin films across a wide spectrum of temperatures which indicated that nickel vacancies were responsible for the observed emission in the produced sample [41]. The photoluminescence (PL) intensities of NSO thin films were found to be fluctuating with the influence of deposited substrate temperature and time, as shown in Fig. 7(a) and

Fig. 7 The photoluminescence (PL) measured spectra for (**a**) NiSnO₃ (NSO) thin films deposited at different deposition temperatures and (**b**) of spray times at the excitation wavelengths 300 and 350 nm
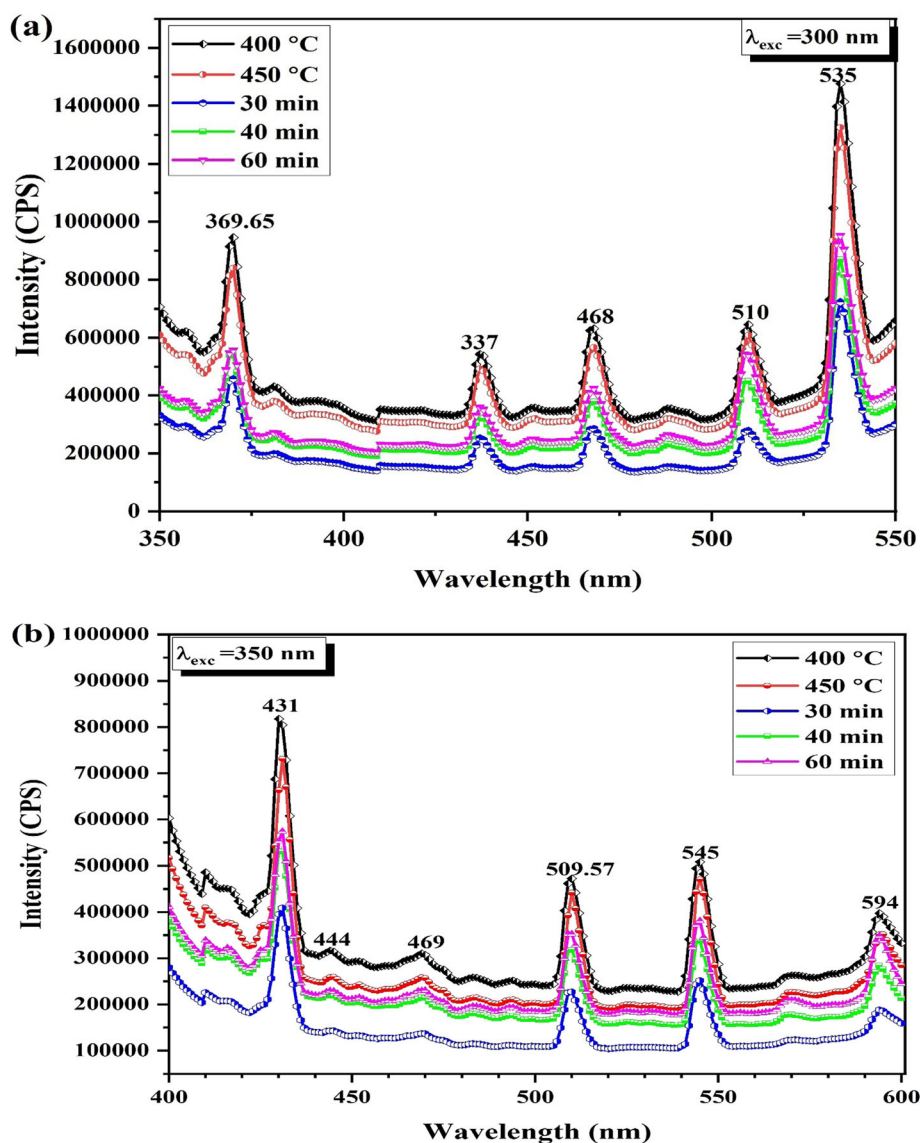

(b) due to the structural characteristics. This finding demonstrates that the utilization of deposited NSO thin films can enhance the efficiency of photoinduced electron and hole separation while concurrently inhibiting the undesired recombination process of photogenerated electrons and holes within NSO that which supportive the idea to use the prepared samples as a photo-sensor candidate.

3.6. UV-illuminations photo-response measurements

The change in the behavior of the sample's resistance measurement is recorded directly by the (Tekpower TP4000zc-RS232) multimeter connected to the PC. The utilized UV-lamp's ($\lambda = 254$ nm, $I = 5$ mW/cm^2) incident photon energy is 4.88 eV, which is higher than the examined samples of 3.75 eV energy gap.

So, the creation of electron–hole pairs continues, resulting in an overabundance of free carriers, which induces photocurrent that allows the abrupt decrease in sample dark resistance. To calculate the rate of decrease/increase of the sample resistance corresponding to [ON (light)/OFF (dark)] cycle, three (ON/OFF) cycles are enlarged by retracing the recoded data using a charting program for the prepared samples. The effect of the deposition temperatures (400, 450 & 500 °C) on the photo-response is investigated and as shown in Fig. 8 the samples deposited at 500 °C and 60 min of spray time recorded the highest photo-response and recovery when exposed to the (ON/OFF) UV cycle of illumination. When the samples are subjected to the UV radiation, they exhibit a high photo-response with an abrupt drop in the resistance from overload (O.L. MΩ) range to ≈ 2 M Ohms after 63 s of illumination. This highly photo-response is related to the well-

Fig. 8 The recorded photo-response of three UV light exposure cycles with (ON-, light mode / OFF-, dark mode) for the films deposited at 500 °C and 60 min of spray time
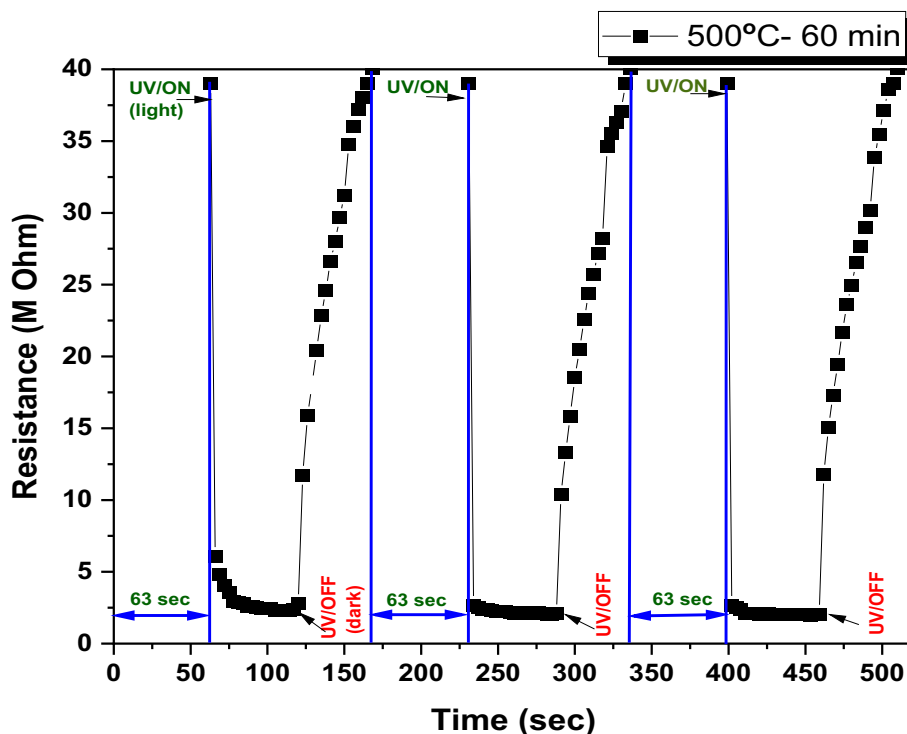
constructed hexagonal pores structure at the surface of the prepared samples as shown in FESEM and PL sections (see Figs. 5(e) & 7(a) and (b)). Since this surface morphology allows the UV light to penetrate and interact with more active sites within the film, it enhances the electron/hole pair generation process and improves the samples conductivity.

The samples prepared at lower temperatures of 400 and 450 °C recorded no discriminative photo-response effect during the UV-(ON/OFF) illumination cycles like that registered for the sample deposited at 500 °C and 60 min of spray time. This vanishing of a well-recorded photo-response for these samples may be related to its both closed & lower surface topography, as seen from FESEM graphs (see Fig. 5(a) and (b)) and the high adsorption of oxygen on the film surface. The constant resistance values of the samples after a considerable illumination time can be attributed to the constant photo current arises from the equilibrium state between generation and the recombination process in charge carriers. Also, the recovery to the dark (OFF) resistance value occurs after nearly ∼ 1 min of light turning off.

The effect of the spray time on the photo-response is recorded for the samples deposited at a constant substrate temperature of 500 °C and different spray times of (30, 40 & 60 min) as seen in Fig. 9. Three different (ON/OFF) cycles for the dynamic photo-response were performed for the films deposited at different spray times, showing that the sample deposited at 60 min gave the highest values of

photo-response and recovery as well as the sample resistance loss.

The key characteristic of the ON/OFF figure is the asymmetry of the resistance decrease and rise, which indicates presence of localized intermediate states within the energy gap that obstruct the direct electron/hole recombination as reported in the obtained PL data with the presence of intrinsic defects or oxygen vacancies. This fascinating property of UV light response makes the tested samples of NiSnO₃ easy to functionalize and work as a photo-sensor for hazardous illumination.

4. Conclusions

NiSnO₃ bimetal oxide thin films are prepared on glass substrates by a low cost pulsed spray pyrolysis technique at different substrate temperatures and spray times. Structural properties are determined by XRD, which confirmed a polycrystalline nature for the deposited films. Raman spectroscopy confirms the formation of a pure NSO thin film. Morphological studies of the film surface were examined by FESEM showed a membrane like-structure with a different diameter size of hexagonal pores. Optical measurements represented a high transparency of 65% for the films deposited at lower spray times, with an estimated optical bandgap range between 3.59 and 3.72 eV. The UV emission in NSO is characterized by two distinct PL peaks at 369.65 and 381.46 nm, which correspond to band-to-

Fig. 9 The recorded photo-response of three UV light exposure cycles with (ON-, light mode / OFF-, dark mode) for the films deposited at 500 °C and different spray times of (30, 40 & 60) min
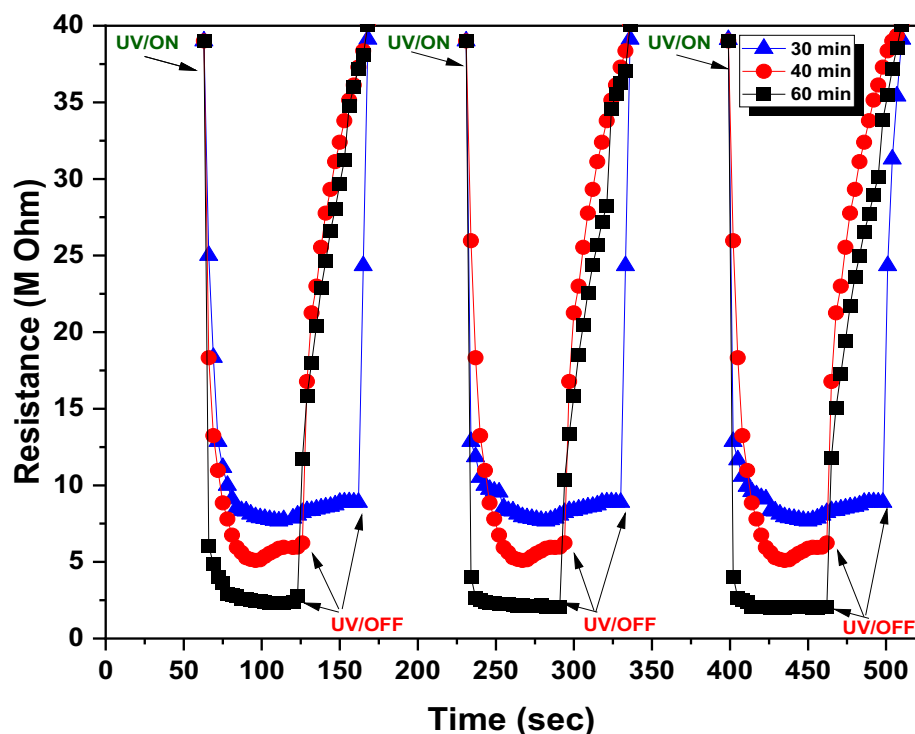
band and exciton recombination, respectively, which occur within the wide bandgap of NSO and are consistent with the results of optical analysis. The UV-illumination photo-response/recovery mechanisms analysis manifested that the preparation conditions are playing an important role in the change of the film resistance. The samples prepared at substrate temperature of 500 °C and 60 min showed a highly dynamic photo-response, which makes it a suitable candidate to use as a photo-sensor device for harmful rays like UV light.

Data availability The authors confirm that the data supporting the findings of this study are available within the article and its supplementary materials.

Declarations

Conflict of interest The authors state that there is no conflict of interest.

Ethics approval On behalf of all authors, the corresponding author states that there are no ethical issues, and the research is not involving the studies on human or their data.

References

[1] A Boukhachem, R Boughalmi, M Karyaoui, A Mhamdi, R Chtourou, K Boubaker and M Amlouk *J. Mater. Sci. Eng. B* **188** 72 (2014).

[2] M Obaida, I Moussa, S Hassan, H Afify and A Abouelsayed *Egypt. J. Chem.* **63** 2331 (2020).

[3] S B Sundararaj, S Tamilarasan, K Kadirvelu and S Thangavelu *Appl. Surf. Sci.* **612** 155785 (2023).

[4] X Wang, W Liu, C Wang, S Zhang, M Ding and X Xu *Sens. Actuators B Chem.* **344** 130190 (2021).

[5] M Annalakshmi, S Sumithra, S M Chen, T W Chen and X H Zheng *New J. Chem.* **44** 10604 (2020).

[6] K Qu, S Wang, W He, H Yin, L Wang and Y Zheng *Solid State Sci.* **135** 107070 (2023).

[7] A A Yadav and U Chavan *Thin Solid Films* **634** 33 (2017).

[8] P Ahuja, S K Ujjain, R K Sharma and G Singh *RSC Adv.* **4** 57192 (2014).

[9] F Bao, Z Zhang, X Liu and X Zhao *RSC Adv.* **4** 38073 (2014).

[10] N A Mala, M A Dar, S Sivakumar, K S Bhat, G N Sinha and K M Batoo *J. Mater. Sci. Mater. Electron.* **33** 11582 (2022).

[11] T Peng, S Fang, C Liu, X Hou, H Yang, R Luo, Q Yu, Y Lu, H Yan and Y Luo *Dalton Trans.* **46** 7451 (2017).

[12] E Sohouli, K Adib, B Maddah and M Najafi *Ceram. Int.* **48** 295 (2022).

[13] Y Xie *Inorg. Nano-Met. Chem* **52** 548 (2022).

[14] M Obaida, A M Fathi, I Moussa and H Afify *J. Mater. Res.* **37** 2282 (2022).

[15] M Obaida, I Moussa and M Boshta *Int. J. Chem. Tech. Res.* **8** 239 (2015).

[16] S Asgharizadeh, M Lazemi, S M Rozati, M Sutton and S Bellucci *Surf. Interface Anal.* **53** 125 (2021).

[17] X H Wu, Y D Wang, H L Liu, Y F Li and Z L Zhou *Mater. Lett.* **56** 732 (2002).

[18] T Athar, M Abdelaal, Z Khatoon, A Kumar, A Razzaq, A A Khan, H Fouad, S A Ansari and Z A Ansari *Sens. Mater.* **27** 563 (2015).

[19] A Mhamdi, R Dridi, A Arfaoui, C Awada, M Karyaoui, I Velasco-Davalos, A Ruediger and M Amlouk *Opt. Mater* **47** 386 (2015).

[20] P Saranya and S Selladurai *J. Mater. Sci.* **53** 16022 (2018).

[21] W Yude, S Xiaodan, L Yanfeng, Z Zhenlai and W Xinghui *Solid State Electron.* **44** 2009 (2000).

[22] B Venkatesh and S Kalyane *J. Impact Factor* **5** 13 (2014).

[23] Y Barakat and R Tali *Chem. Mater. Res.* **8** 28 (2016).

[24] D Kan, T Terashima, R Kanda, A Masuno, K Tanaka, S Chu, H Kan, A Ishizumi, Y Kanemitsu and Y Shimakawa *Nat. Mater.* **4** 816 (2005).

[25] H Takashima, K Shimada, N Miura, T Katsumata, Y Inaguma, K Ueda and M Itoh *Adv. Mater.* **21** 3699 (2009).

[26] Y Yamada and Y Kanemitsu *J. Lumin.* **133** 30 (2013).

[27] J Chen, M Zou, J Li, W Wen, L Jiang, L Chen, Q Feng and Z Huang *RSC Adv.* **6** 85374 (2016).

[28] C Mrabet, M B Amor, A Boukhachem, M Amlouk and T Manoubi *Ceram. Int.* **42** 5963 (2016).

[29] X Li and C Wang *RSC Adv.* **2** 6150 (2012).

[30] S Mehraj, M S Ansari and A A Al-Ghamdi *Mater. Chem. Phys.* **171** 109 (2016).

[31] P Patil, R Kawar, T Seth, D Amalnerkar and P Chigare *Ceram. Int.* **29** 725 (2003).

[32] S Nkosi, B Yalisi, D Motaung, J Keartland, E Sideras-Haddad, A Forbes and B W Mwakikunga *Appl. Surf. Sci.* **265** 860 (2013).

[33] D Dubal, A Jagadale, S Patil and C Lokhande *Mater. Res. Bull.* **47** 1239 (2012).

[34] R Dridi, A Mhamdi, A Labidi, A Amlouk and M Amlouk *Mater. Chem. Phys.* **182** 498 (2016).

[35] N Ghobadi *Int. Nano Lett.* **3** 2 (2013).

[36] M Ardyanian, M Moeini and H A Juybari *Thin Solid Films* **552** 39 (2014).

[37] M Öztas *Chin. Phys. Lett.* **25** 4090 (2008).

[38] F G El Desouky, M Saadeldin and W H Eisa *Surf. Interfaces* **38** 102749 (2023).

[39] M M Khan, S A Ansari, M I Amal, J Lee and M H Cho *Nanoscale* **5** 4427 (2013).

[40] A Tripathi and R Shukla *Bull. Mater. Sci.* **37** 417 (2014).

[41] D Jiang, J Qin, X Wang, S Gao, Q Liang and J Zhao *Vacuum* **86** 1083 (2012).